**Acta Mechanica manuscript No.**
(will be inserted by the editor)

**M. Ozdemir · S. Sadamoto · S. Tanaka · S. Okazawa · T.T. Yu · T.Q. Bui**

# Application of 6-DOFs meshfree modeling to the linear buckling analysis of stiffened plates with curvilinear surfaces

Received: date / Accepted: date

**Abstract** Buckling analysis of stiffened plates including curvilinear surfaces is carried out by an effective meshfree model. The buckling loads and modes computed by the present method are analyzed. Six degrees of freedom (6-DOFs) curved shell meshfree formulation in convected coordinate system including a drilling rotation component is employed, which enables the assembly of curved shells for the modeling of more complex structures. By this formulation, assembly of any arbitrary shape of geometry can be modeled in convected coordinates; while the 5-DOFs shell formulation suffers from the modeling of shell assemblies. Particularly, curved shells with straight stiffeners, plates with curvilinear stiffeners are considered. Furthermore, a twisted T-shaped structure that is both web and flange have curvilinear geometry is analyzed. A meshfree discretization is employed, with which the reproducing kernel particle method (RKPM) is used as the meshfree interpolant. A boundary singular kernel (SK) method is adopted to precisely impose essential boundary condition (BC) and to model folded shell geometries. The accuracy and effectiveness of the proposed method are demonstrated through several shell buckling problems for stiffened plate structures with curvilinear surfaces. The obtained meshfree results are compared with the linear and quadratic shell element results of Finite Element Method FEM (ANSYS) and discussed.

**Keywords** Buckling · Stiffened plates · Curvilinear surfaces · Convected coordinates · RKPM

M. Ozdemir
Department of Naval Architecture and Marine Engineering, Ordu University, Turkey
E-mail: muratozdemir@odu.edu.tr

S. Sadamoto
Graduate School of Engineering, Hiroshima University, Japan,
Current adress: Fujitsu Limited, Japan
E-mail: shota.sadamoto@gmail.com

S. Tanaka
Graduate School of Engineering, Hiroshima University, Japan
E-mail: satoyuki@hiroshima-u.ac.jp

S. Okazawa
Division of Mechanical Engineering, Faculty of Engineering, University of Yamanashi, Japan
E-mail: sokazawa@yamanashi.ac.jp

T.T. Yu
Department of Engineering Mechanics, Hohai University, China
E-mail: tiantangyu@hhu.edu.cn

T.Q. Bui
Department of Civil and Environmental Engineering, Tokyo Institute of Technology, Japan
E-mail: bui.t.aa@m.titech.ac.jp

## 1 Introduction

The stiffened panels are common and important structural members in many engineering applications including ship hulls, bridges and storage tanks. The combination of plate and stiffeners inherently provides higher strength to weight ratios, and this advantage brings with several research works dealing with buckling analysis by FEM [1–4], analytical [5, 6], and semi-analytical methods [7–9]. In addition to buckling analysis, the ultimate strength of stiffened plates has also been investigated mainly by FEM [10–13], and semi-analytical estimation methods [14, 15] during the last few decades. Nonlinear collapse behavior of the stiffened curved plates was also examined and design formulae were proposed by Seo *et al.* [16]. A comprehensive reference textbook covering buckling and ultimate strength of plates and stiffened plates was recently published by Yao and Fujikubo [17]. Monotonously increasing demands on the performance of the structures, especially in the aerospace and modern shipping industry, push the engineers to design unconventional but efficient structures to meet the marginal requirements. Such demands also trigger development of production methods. The development of manufacturing and material technologies enables the production and utilization of the structural arrangement of complex geometries; such as a plate with curvilinear stiffeners. Kapania *et al.* [18] introduced the concept of curvilinear stiffeners to show that the curvilinear stiffeners can provide lighter weight than the panels with straight stiffeners in some cases. Furthermore, Kapania and his colleagues performed static, buckling and vibration analysis of homogeneous plates with curvilinear stiffeners by element-free Galerkin method [19], FEM [20], and for composite curvilinearly stiffened plates by FEM [21]. The structural optimization of plate-curvilinear stiffener arrangements has been investigated in Refs. [22,23]. Recently, Qin and his colleagues examined the static and dynamic behavior of curvilinearly stiffened plates [24], and the free vibration of curvilinearly stiffened shells [25] employing isogeometric analysis method. In those works, stiffeners were modeled by beam formulation. The structural efficiency of the stiffened ship panels with unconventional stiffener cross-section (Y-type) was examined by Leheta *et al.* [26]. On the other hand, Liew and his colleagues performed a series of buckling and vibration analyses of plates and plate assemblies based on first order shear deformation theory by RKPM [27], radial basis function method [28] and meshfree Galerkin methods [29, 30].

Above references show that FEM with shell elements is the most common approach for simulation of stiffened panels. Furthermore, linear element formulation was usually adopted due to the lower computational effort. However, linear shell elements sometimes become vulnerable to shear locking; particularly in the approximation of curvilinear surfaces. In addition, conventional FEM with linear elements suffers from the non-smooth stress-strain field. Special procedures, *e.g.*, consecutive interpolation procedure [31], are required to eliminate such non-smooth stress-strain field. Consecutive interpolation procedure can also be improved for evaluating fracture parameters [32].

Meshfree methods, an alternative discretization method, can easily deal with the trouble caused by shear locking owing to the higher order approximation functions. Our research group therefore studied meshfree fracture [33–35] and buckling problems [36–38]. Buckling analyses were carried out for isotropic cylindrical shells [36] and curvilinearly stiffened structural plates [37] by employing 5-DOFs shell formulation. In Ref. [37], the curvilinear stiffeners were not modeled explicitly; but the out of plane displacements were suppressed along the plate-stiffener connections. In addition, linear buckling behavior of continuous stiffened plates was studied in detail by meshfree RKPM with 6-DOFs flat shell formulation introducing drilling rotation component by the present authors [38]. It was shown that the 6-DOFs shell formulation is efficient in simulating flat plate-flat stiffener interaction. The compatible displacement field was ensured by an efficient coordinate transformation rule and Multi-Point Constraint (MPC) technique. Chen and Wang [39] proposed constrained reproducing kernel particle formulation addressing singular moment matrix when the RKs are produced in Cartesian coordinates for complex geometries; and the displacement compatibility was ensured in Ref. [39].

Moreover, present authors performed geometrical nonlinear analysis of folded plate structures using 6-DOFs meshfree method in [40]. However, MPC was adopted to impose essential BCs, the accuracy around the boundaries is sometimes deteriorated as reported in [41]. The influence of order of original kernel function, *i.e.*, higher order versions of present formulation, on the stress and error norms for the geometrically nonlinear analysis was also assessed by Ref. [41]. The accuracy of an eigenvalue analysis, *e.g.*, vibration and linear buckling problems, is worsen by the numerical error around the BCs. Hereby, a powerful essential BCs enforcement technique, boundary SK approach [42], is introduced to impose the Kronecker Delta function property. In the present SK approximation, singular kernels are only

generated at the boundary nodes, where the essential BCs are applied on or coinciding boundary nodes; not the interior nodes. According to the authors' knowledge, application of accurate buckling analysis for curvilinearly stiffened plates as well as complex geometries by the meshfree shell formulation has not been reported yet. Kapania and his colleagues as well as Qin and his colleagues modeled stiffeners on the basis of beam formulation in Refs. [20, 21] and Refs. [24, 25], respectively. Such modeling may be sufficient when stiffener size is relatively small. On the other hand, local buckling of stiffeners and mother (base) shells may take place when the stiffener size is relatively large. In this case, beam formulation suffers from representing local stiffener buckling. We therefore model both stiffeners and mother shells by 6-DOFs shell formulation in convected coordinates to effectively simulate the plate-stiffener interaction as well as local buckling of the stiffeners. A smooth stress-strain field over the whole domain is achieved by higher order continuous interpolation functions for the approximation of physical values and the shell geometry in a similar fashion with isoparametric FEM. In the numerical integration, physical values are smoothed on the basis of strain smoothing approaches. Sub-domain stabilized conforming integration (SSCI) [43–46] method is adopted to effectively simulate higher stress gradients along the plate-stiffener connections. Wang and Peng [44] performed the numerical integration of weak form by SSCI with smoothed measures of rotation and curvature. Wang and Wu [46] proposed nesting sub-domain gradient smoothing integration (NSGSI) based upon SSCI, and the stiffness matrix can be integrated exactly for any quadratic field. As for the remaining regions, stabilized conforming nodal integration (SCNI) method proposed by Chen *et al.* [47] is applied. By employing advanced numerical integration methods, the stiffness matrices can be derived more effectively, which results in accurate evaluation of buckling loads and modes.

This paper is organized as follows: In Section 2, 6-DOFs shell formulation is briefly described. Meshfree discretization and introduction of drilling rotation component are explained in Section 3. In Section 4, modeling of plate-stiffener assemblies and numerical integration techniques are briefly explained. Accuracy and effectiveness of the proposed method are demonstrated through numerical examples in Section 5. The meshfree results are also compared with linear and quadratic shell elements of FEM (ANSYS). The results are critically investigated and discussed. Concluding remarks are drawn in Section 6.

## 2 6-DOFs shell formulation and approximations

6-DOFs meshfree formulation and discretization including curvilinear surfaces are used. They are briefly reviewed here for the analysis of linear buckling problems. 6-DOFs shell formulation considers both in-plane and out-plane deflections as well as drilling rotation component. This modeling makes possible to solve buckling problems of plate - stiffeners combinations considering transverse shear strains effectively. A schematic illustration of coordinate transformation between global Cartesian coordinates and convected coordinates is given in Fig.1. In the given figure, $\boldsymbol{X}$=$(X_1, X_2, X_3)$ is a position vector in the Cartesian coordinates, and $\boldsymbol{r}$=$(r_1, r_2, r_3)$ is that in the convected coordinates. 6-DOFs, including translation ($u_1$, $u_2$, $u_3$) and rotation ($\theta_1$, $\theta_2$, $\theta_3$) components, are considered. In the present study, all surfaces are firstly created in convected coordinate system ($r_1, r_2$ plane), then mapped into Cartesian coordinates. All derivations can, therefore, be performed in the convected coordinates. Scattered nodes can be set on the mid-thickness plane either in regular or irregular pattern. The nodal values in the two coordinate systems have a one-to-one correspondence.

The displacement of a point on a shell surface can be written in terms of rotation angles and the translation of mid-thickness plane as:

$$\boldsymbol{u} = \boldsymbol{u}_{\mathrm{mid}} + \frac{r_3}{2} t_{\mathrm{h}} (-\beta_1 \boldsymbol{V}_2 + \beta_2 \boldsymbol{V}_1), \tag{1}$$

where $\beta_1$ and $\beta_2$ are the rotation angles in terms of the tangential unit vectors $\boldsymbol{V}_1$ and $\boldsymbol{V}_2$. Right hand side term, $-\beta_1 \boldsymbol{V}_2 + \beta_2 \boldsymbol{V}_1$, denotes the rotation of director, $\boldsymbol{V}_3$. Tangential units, $\boldsymbol{V}_i$ and the unit vectors, $\boldsymbol{e}_i$ in Cartesian coordinates have the following relation:

$$\boldsymbol{V}_2 = \frac{\boldsymbol{V}_3 \times \boldsymbol{e}_1}{|\boldsymbol{V}_3 \times \boldsymbol{e}_1|}, \tag{2}$$

$$\boldsymbol{V}_1 = \boldsymbol{V}_2 \times \boldsymbol{V}_3. \tag{3}$$

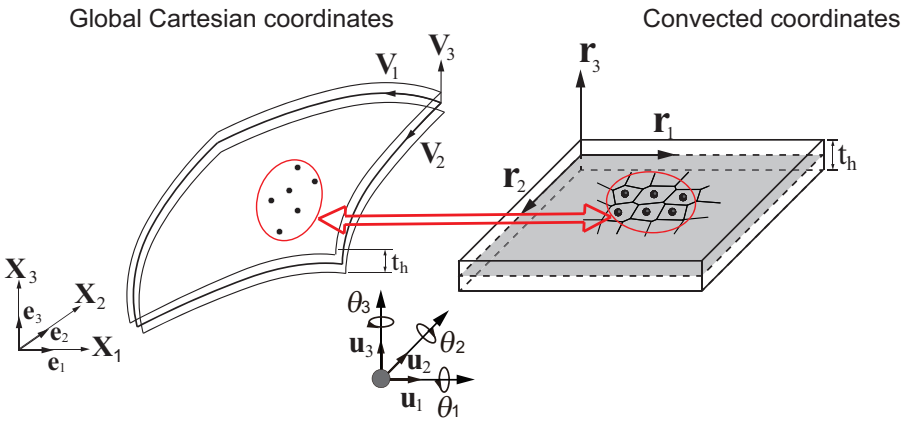


**Fig. 1** A schematic illustration of a shell with 6-DOFs and mapping for curvilinear geometry.

Considering Eq. (1), a similar expression can be written for position of a point on shell surface as:

$$\boldsymbol{X} = \boldsymbol{X}_{\text{mid}} + \frac{r_3}{2} t_{\text{h}} \boldsymbol{V}_3, \tag{4}$$

where $\boldsymbol{X}_{\text{mid}}$ is a position vector on the mid-thickness plane of the curved shell in the Cartesian coordinates. Covariant basis vectors, $\boldsymbol{G}_i$ can be readily derived by differentiating position vector with respect to convected coordinates as:

$$\boldsymbol{G}_i = \frac{\partial \boldsymbol{X}}{\partial r_i}. \tag{5}$$

To meet the Kronecker delta property, contravariant basis vectors are derived as:

$$\boldsymbol{G}^i = \frac{\boldsymbol{G}_j \times \boldsymbol{G}_k}{\boldsymbol{G}_i \cdot (\boldsymbol{G}_j \times \boldsymbol{G}_k)}, \tag{6}$$

where $(i, j, k)$=(1,2,3),(2,3,1),(3,1,2) in Eq. (6). Once giving the relations between base vectors, we can proceed explicit form and approximation of displacements. Eq. (1) can be expressed in explicit form as:

$$\boldsymbol{u} = \left\{ \begin{array}{c} u_1 \\ u_2 \\ u_3 \end{array} \right\} = \left\{ \begin{array}{l} u_{\text{mid}1} - \frac{r_3}{2} t_{\text{h}} \beta_1 \boldsymbol{V}_{2(1)} + \frac{r_3}{2} t_{\text{h}} \beta_2 \boldsymbol{V}_{1(1)} \\ u_{\text{mid}2} - \frac{r_3}{2} t_{\text{h}} \beta_1 \boldsymbol{V}_{2(2)} + \frac{r_3}{2} t_{\text{h}} \beta_2 \boldsymbol{V}_{1(2)} \\ u_{\text{mid}3} - \frac{r_3}{2} t_{\text{h}} \beta_1 \boldsymbol{V}_{2(3)} + \frac{r_3}{2} t_{\text{h}} \beta_2 \boldsymbol{V}_{1(3)} \end{array} \right\}. \tag{7}$$

Here, $\boldsymbol{V}_{i(j)}$ denotes dot product of unit vectors $\boldsymbol{V}_i$ and $\boldsymbol{e}_j$. The displacement of a point on the shell surface is approximated by RK functions as:

$$\boldsymbol{u}(\boldsymbol{r}) = \sum_{I=1}^{NP} \psi_I(\boldsymbol{r}) \left( \boldsymbol{u}_{\text{mid}I} + \frac{r_3}{2} t_h \boldsymbol{V}_{3I} \right), \tag{8}$$

where $\psi_I(\boldsymbol{r})$ represents the RK functions. On the other hand, $\boldsymbol{u}_{\text{mid}I}$ stands for the coefficient vector for each node on the mid-thickness plane and $NP$ is the total number of nodes to be used for the approximation. This approximation can be expressed in explicit form as:

$$\boldsymbol{u} = \sum_{I=1}^{NP} \begin{bmatrix} \psi_I & 0 & 0 & -\frac{r_3}{2} t_{\text{h}} \psi_I \boldsymbol{V}_{2(1)} & \frac{r_3}{2} t_{\text{h}} \psi_I \boldsymbol{V}_{1(1)} \\ 0 & \psi_I & 0 & -\frac{r_3}{2} t_{\text{h}} \psi_I \boldsymbol{V}_{2(2)} & \frac{r_3}{2} t_{\text{h}} \psi_I \boldsymbol{V}_{1(2)} \\ 0 & 0 & \psi_I & -\frac{r_3}{2} t_{\text{h}} \psi_I \boldsymbol{V}_{2(3)} & \frac{r_3}{2} t_{\text{h}} \psi_I \boldsymbol{V}_{1(3)} \end{bmatrix} \left\{ \begin{array}{c} u_{1I} \\ u_{2I} \\ u_{3I} \\ \beta_{1I} \\ \beta_{2I} \end{array} \right\} = \sum_{I=1}^{NP} \boldsymbol{\Psi}_I \boldsymbol{U}_I, \tag{9}$$

where $\boldsymbol{U}_I$ is 5-DOFs coefficient vector. So far, shell kinematics and approximation of displacements in terms of RK functions were briefly described. As for the details of the shell kinematics as well as approximation of physical values and curved shell surface, see Ref. [36].

2.1 Relationship between rotation components and rotation angles

The relationship between the rotation angles and rotation components including drilling rotation angle, $\beta_3$, is introduced here. The rotation vector of directors, $\boldsymbol{\omega}$, is schematically illustrated in Fig.2.

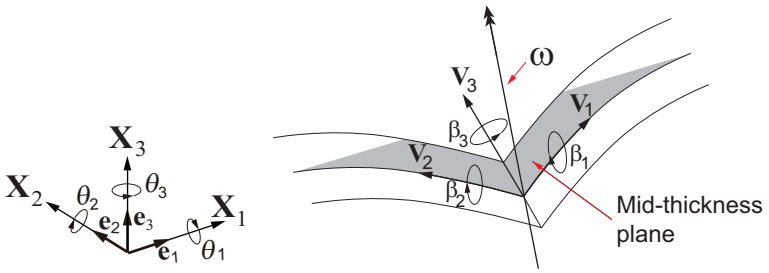


**Fig. 2** Schematic illustration of the rotation vector $\boldsymbol{\omega}$.

The rotation vector of directors, $\boldsymbol{\omega}$ is expressed considering rotation angles, rotation components and unit vectors as:

$$\boldsymbol{\omega} = \beta_i \boldsymbol{V}_i = \theta_j \boldsymbol{e}_j. \tag{10}$$

The rotation angles then can be written as:

$$\beta_i = \boldsymbol{V}_i \cdot \boldsymbol{e}_j \theta_j = \boldsymbol{V}_{i(j)} \theta_j. \tag{11}$$

The relationship is written in explicit form as follows:

$$\left\{ \begin{array}{c} \beta_1 \\ \beta_2 \\ \beta_3 \end{array} \right\} = \left[ \begin{array}{ccc} \boldsymbol{V}_{1(1)} & \boldsymbol{V}_{1(2)} & \boldsymbol{V}_{1(3)} \\ \boldsymbol{V}_{2(1)} & \boldsymbol{V}_{2(2)} & \boldsymbol{V}_{2(3)} \\ \boldsymbol{V}_{3(1)} & \boldsymbol{V}_{3(2)} & \boldsymbol{V}_{3(3)} \end{array} \right] \left\{ \begin{array}{c} \theta_1 \\ \theta_2 \\ \theta_3 \end{array} \right\}. \tag{12}$$

Then, the kinematic relations can be rewritten considering Eq. (12) as:

$$\boldsymbol{u} = \boldsymbol{u}_{\mathrm{mid}} + \frac{r_3}{2} t_{\mathrm{h}} \left( -(\boldsymbol{\theta} \cdot \boldsymbol{V}_1) \boldsymbol{V}_2 + (\boldsymbol{\theta} \cdot \boldsymbol{V}_2) \boldsymbol{V}_1 \right), \tag{13}$$

where $\boldsymbol{V}_i = \{V_{i(1)}\ V_{i(2)}\ V_{i(3)}\}$ and $\boldsymbol{\theta} = \{\theta_1\ \theta_2\ \theta_3\}^T$. The derivatives of the displacement vector are obtained as:

$$\frac{\partial \boldsymbol{u}}{\partial r_i} = \frac{\partial \boldsymbol{u}_{\mathrm{mid}}}{\partial r_i} + \frac{r_3}{2} t_{\mathrm{h}} \left( -\frac{\partial}{\partial r_i}(\boldsymbol{\theta} \cdot \boldsymbol{V}_1) \boldsymbol{V}_2 - (\boldsymbol{\theta} \cdot \boldsymbol{V}_1) \frac{\partial \boldsymbol{V}_2}{\partial r_i} + \frac{\partial}{\partial r_i}(\boldsymbol{\theta} \cdot \boldsymbol{V}_2) \boldsymbol{V}_1 - (\boldsymbol{\theta} \cdot \boldsymbol{V}_2) \frac{\partial \boldsymbol{V}_1}{\partial r_i} \right), (i = 1, 2) \tag{14}$$

$$\frac{\partial \boldsymbol{u}}{\partial r_3} = \frac{1}{2} t_{\mathrm{h}} (-(\boldsymbol{\theta} \cdot \boldsymbol{V}_1) \boldsymbol{V}_2 + (\boldsymbol{\theta} \cdot \boldsymbol{V}_2) \boldsymbol{V}_1). \tag{15}$$

## 3 Meshfree discretization for buckling problems

Buckling problem is related with energy principles so that buckling equations can be derived by Principle of Virtual Work. Thus, the general form of virtual work equation is written as:

$$\int_V \boldsymbol{S} : \delta \boldsymbol{E} dV = \int_S \overline{\boldsymbol{t}} \delta \overline{\boldsymbol{u}} dS, \tag{16}$$

where $\boldsymbol{S}$ stands for second Piola-Kirchhoff stress tensor and $\boldsymbol{E}$ is Green-Lagrange strain tensor, while $\overline{\boldsymbol{t}}$ and $\overline{\boldsymbol{u}}$ denote traction forces and corresponding displacement terms, respectively. $\delta$ is a variational

operator. $V$ is the volume of the shell and $S$ is the shell surface, where traction force is applied on. At first, a linear static analysis has to be performed to obtain pre-buckling stresses under a reference external load. Once the pre-buckling stresses are obtained for the reference loads, the left hand side of Eq. (16) can be decomposed into linear and non-linear parts, which are associated with linear and non-linear parts of strain tensor as follows :

$$\begin{aligned}\boldsymbol{E} &= \frac{1}{2}\left\{\left(\boldsymbol{G}_i \cdot \frac{\partial \boldsymbol{u}}{\partial r_j} + \boldsymbol{G}_j \cdot \frac{\partial \boldsymbol{u}}{\partial r_i}\right) + \left(\frac{\partial \boldsymbol{u}}{\partial r_i} \cdot \frac{\partial \boldsymbol{u}}{\partial r_j}\right)\right\}\boldsymbol{G}^i \otimes \boldsymbol{G}^j \\ &= \left(\varepsilon_{\mathrm{L}ij} + \varepsilon_{\mathrm{NL}ij}\right)\boldsymbol{G}^i \otimes \boldsymbol{G}^j = \boldsymbol{\varepsilon}_{\mathrm{L}} + \boldsymbol{\varepsilon}_{\mathrm{NL}}. \end{aligned} \tag{17}$$

In the linear static analysis, all measures of stresses and strains are equivalent; and the left hand side of Eq. (16) becomes equivalent to total strain energy, which is also decomposed as follows.

$$\Pi = \Pi_L + \Pi_{NL}, \tag{18}$$

where, $\Pi_L$ and $\Pi_{NL}$ are associated with linear, $\boldsymbol{\varepsilon}_{\mathrm{L}}$ and non-linear, $\boldsymbol{\varepsilon}_{\mathrm{NL}}$ strains, which are respectively expressed as:

$$\Pi_L = \frac{1}{2}\int_V \boldsymbol{\sigma} : \boldsymbol{\varepsilon}_L dV, \tag{19}$$

$$\Pi_{NL} = \frac{1}{2}\int_V \boldsymbol{\sigma}_0' : \boldsymbol{\varepsilon}_{NL} dV. \tag{20}$$

Assuming plane stress condition, in-plane stresses increase with respect to critical load parameter, $\lambda$, which states the additional loads cannot be sustained by in-plane displacements any longer. At this moment, applying the stationary condition for $\Pi$ with respect to displacement vector, the final form of buckling equation can be written as:

$$\int_V \boldsymbol{\sigma} : \delta\boldsymbol{\varepsilon}_{\mathrm{L}} dV + \lambda \int_V \boldsymbol{\sigma}_0' : \delta\boldsymbol{\varepsilon}_{\mathrm{NL}} dV = 0, \tag{21}$$

where $\boldsymbol{\varepsilon}_{\mathrm{L}}$ and $\boldsymbol{\varepsilon}_{\mathrm{NL}}$ stand for the linear and nonlinear strain tensors, respectively. $\boldsymbol{\sigma}$ and $\boldsymbol{\sigma}_0'$ denote the Cauchy stress tensor and pre-buckling stress tensor, respectively. The details of the strain tensors as well as stress tensors were defined in Ref. [36].

### 3.1 Introduction of drilling rotation component

Due to difficulties in modeling of assembled structures by 5-DOFs shell formulation, the relationship between rotation angles and rotation components including drilling rotation component has been defined in the previous section. The drilling rotation component in the curved shell formulation is introduced to total system by means of penalty energy, $Q_T$, based on the idea of Kanok-Nukulchai [48]. The penalty energy can be written as:

$$Q_T = \kappa_T \int_V C^{1212}\left[\beta_3 |\boldsymbol{G}_1 \times \boldsymbol{G}_2| - \frac{1}{2}\left(\boldsymbol{G}_2 \cdot \frac{\partial \boldsymbol{u}}{\partial r_1} - \boldsymbol{G}_1 \cdot \frac{\partial \boldsymbol{u}}{\partial r_2}\right)\right]^2 dV, \tag{22}$$

where $\kappa_T$ is a parameter for the penalty energy. It is taken as 0.1 as suggested by Ref. [48] to prevent spurious torsional mode. In the case of rigid body rotation, the penalty energy must vanish. On the other hand, $C^{1212}$ is related shear term in the elastic constants tensor. $\beta_3$ is the virtual in-plane rotation. The virtual distortion caused by $\beta_3$ is given as:

$$\varepsilon_{\beta_3} = \left[\beta_3 |\boldsymbol{G}_1 \times \boldsymbol{G}_2| - \frac{1}{2}\left(\boldsymbol{G}_2 \cdot \frac{\partial \boldsymbol{u}}{\partial r_1} - \boldsymbol{G}_1 \cdot \frac{\partial \boldsymbol{u}}{\partial r_2}\right)\right]\boldsymbol{G}_1 \otimes \boldsymbol{G}_2, \tag{23}$$

and the corresponding virtual stress is:

$$R_{\beta_3} = 2\kappa_T\, C^{1212}\varepsilon_{\beta_3}\boldsymbol{G}^1 \otimes \boldsymbol{G}^2. \tag{24}$$

The virtual energy $\delta Q_T$ due to the virtual rotation is added to Eq. (21). Finally, a discrete equation of the eigenvalue problem is derived as:

$$(\boldsymbol{K}_{\mathrm{L}} + \lambda \boldsymbol{K}_{\mathrm{NL}})\boldsymbol{W} = 0, \tag{25}$$

where $\boldsymbol{K}_{\mathrm{L}}$ is the stiffness matrix associated with linear terms:

$$\boldsymbol{K}_{\mathrm{L}} = \int_V \boldsymbol{B}_{\mathrm{L}}^T \boldsymbol{C} \boldsymbol{B}_{\mathrm{L}} dV + \kappa_T \int_V \boldsymbol{B}_{\beta_3}^T C^{1212} \boldsymbol{B}_{\beta_3} dV, \tag{26}$$

and $\boldsymbol{K}_{\mathrm{NL}}$ is the one associated with non-linear terms:

$$\boldsymbol{K}_{\mathrm{NL}} = \int_V \boldsymbol{B}_{\mathrm{NL}}^T \boldsymbol{\sigma}_0' \boldsymbol{B}_{\mathrm{NL}} dV. \tag{27}$$

The details of strain-displacement matrices $\boldsymbol{B}_{\mathrm{L}}$ and $\boldsymbol{B}_{\mathrm{NL}}$ were given by Ref. [36]. Volume integral term $dV$ can be described in terms of covariant base vectors and line elements as $dV = [\boldsymbol{G}_1 \boldsymbol{G}_2 \boldsymbol{G}_3] dr_1 dr_2 dr_3$.

## 4 Modelling of plate-stiffener assemblies

A plate and curvilinear stiffener assembly is schematically illustrated in Fig.3(a). In this figure, $\boldsymbol{e}_i$ and $\boldsymbol{e}_i'$ ($i$=1,2,3) are unit vectors for plate and stiffener parts in their local coordinates, respectively. As can be seen from the given figure, the nodal arrangement might have regular or irregular pattern, but the important thing is the synchronization of the coinciding nodes.

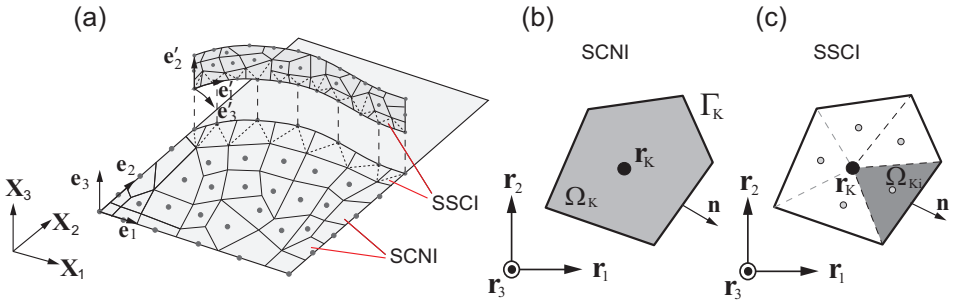


**Fig. 3** Modeling of stiffened plates: (a) assembly of plate and curvilinear stiffener, (b) SCNI, (c) SSCI.

At first, flat shell models are independently generated for the plate and the stiffeners. The support domains of the nodes lie in their own plane, which is conceptually similar to FEs. The approximation of nodal displacements as well as the geometry by RKs are performed independently for each body. As for the modeling of plate-stiffener assemblies, orthogonal transformation of the base vectors for geometry and displacement components is performed. This concept was presented in our previous study, Ref. [38]. After the assembly process, we employ convected coordinates concept, which is similar to Ref. [49], defining any arbitrary shape of geometry from the flat surfaces. At this moment, the displacement components of the coinciding nodes of the bodies are synchronized. SK [42] is set for the coinciding nodes to enforce the displacement constraints. Once SK is set, synchronization could be easily imposed to coinciding nodes of plate and stiffeners regardless of shape of the geometry.

### 4.1 Numerical integration techniques

The SCNI [47] is adopted to derive stiffness matrices. However, for more accurate simulation of higher stress gradients along the plate-stiffener connections, more improved one, SSCI [43–46] is employed for the plate-stiffener connecting nodes. In case of SCNI, Voronoi cells covering the nodes are generated as shown in Fig.3(b). In that figure, $\Omega_K$ denotes Voronoi cell's domain, and $\Gamma_K$ is boundary of the

domain. On the other hand, $\boldsymbol{n}$ represents normal vector of the cell boundary and $\boldsymbol{r}_K$ is the coordinate of $k$-th node. Domain integral is reduced to a contour integral by means of Gauss-Divergence theorem, calculation of interpolation function's derivatives is therefore no longer needed. Physical values can be obtained by interpolation function itself and normal vectors of the boundaries.

The physical values $d_j(\boldsymbol{r})$ ($j$= 1, 2, 3) are smoothed throughout the Voronoi cell, *i.e.*,

$$\tilde{d}_j^h(\boldsymbol{r}_K) = \frac{1}{A_K}\int_{\Omega_K} d_j^h(\boldsymbol{r})\, d\Omega = \sum_{I=1}^{\mathrm{NP}} \frac{1}{A_K}\int_{\Omega_K} \Psi_I(\boldsymbol{r}) d_{jI}\, d\Omega, \tag{28}$$

where ( ˜ ) represents a smoothed physical quantity. The physical value $\tilde{d}_j^h(\boldsymbol{r})$ is averaged over the entire domain $\Omega_K$, and the values are evaluated at node $\boldsymbol{r}_K$. $A_K$ is the area of domain $\Omega_K$ as shown in Fig.3(b). Using Gauss-Divergence theorem, surface integrals are transformed into contour integrals as:

$$\begin{aligned}
\tilde{d}_{j,k}^h(\boldsymbol{r}_K) &= \frac{1}{A_K}\int_{\Omega_K} d_{j,k}^h(\boldsymbol{r})\, d\Omega \\
&= \frac{1}{A_K}\int_{\Gamma_K} d_j^h(\boldsymbol{r}) n_k\, d\Gamma \\
&= \sum_{I=1}^{\mathrm{NP}} b_{Ik}(\boldsymbol{r}_K) d_{jI}, \qquad (29)
\end{aligned}$$

$$b_{Ik}(\boldsymbol{r}_K) = \frac{1}{A_K}\int_{\Gamma_K} \Psi_I(\boldsymbol{r}) n_k\, d\Gamma. \tag{30}$$

As for the SSCI, the Voronoi cells are further partitioned into triangular sub-domains $\Omega_{Ki}$ as shown in Fig.3(c). In sub-domains the physical values are then smoothed as:

$$\begin{aligned}
\tilde{d}_j^h(\boldsymbol{r}_{K_i}) &= \frac{1}{A_{K_i}}\int_{\Omega_{K_i}} d_j^h(\boldsymbol{r})\, d\Omega \\
&= \sum_{I=1}^{\mathrm{NP}} \frac{1}{A_{K_i}}\int_{\Omega_{K_i}} \Psi_I(\boldsymbol{r}) d_{jI}\, d\Omega, \qquad (31)
\end{aligned}$$

where $A_{K_i}$ and $\Gamma_{K_i}$ are the area and the boundary of the sub-domain $\Omega_{K_i}$ in Fig.3(c). The value is averaged within $\Omega_{K_i}$ and is evaluated at the gravity center of the sub-domain. The derivatives of the physical components $\tilde{d}_{j,k}(\boldsymbol{r}_{K_i})$ are evaluated through the following expressions:

$$\tilde{d}_{j,k}^h(\boldsymbol{r}_{K_i}) = \sum_{I=1}^{\mathrm{NP}} b_{Ik}(\boldsymbol{r}_{K_i}) d_{jI}, \tag{32}$$

$$b_{Ik}(\boldsymbol{r}_{K_i}) = \frac{1}{A_{K_i}}\int_{\Gamma_{K_i}} \Psi_I(\boldsymbol{r}) n_k\, d\Gamma. \tag{33}$$

Once deriving the stiffness matrix for the curvilinear surfaces employing convected coordinates, SCNI and SSCI; the stiffness matrix of the plate-stiffener assembly can then be derived in the same manner with Ref. [38].

## 5 Numerical examples and discussions

A series of linear buckling analysis is performed to show the accuracy and effectiveness of the proposed meshfree method with convected coordinate system and advanced numerical integration techniques. As first, shallow shell models with straight stiffeners are analyzed. The shell models without stiffeners, employing 5-DOFs shell formulation, have been previously analyzed by the present authors [36]. A convergence study is performed for one case of stiffened shallow shells. In this case, mother plate

has curvilinear surface but the stiffener is straight. Then, buckling behavior of flat plate models with curvilinear stiffeners is examined. As a final numerical example, a twisted T-shaped model is considered. For this problem, both flange and web have curvilinear surfaces.

As for comparison, the numerical results obtained by the present meshfree method are compared with the reference solutions derived from the FEM. In this study, the commercial FEM package, ANSYS [50] is used. Bilinear general purpose shell elements (Shell181) based on Mindlin-Reissner theory are adopted. This type of element has four nodes and 6-DOFs at each node. Shell181 is well suited for simulating both linear and nonlinear behavior of thin to moderately thick shells with sufficient accuracy and low computational efforts. We have already demonstrated capability of the Shell181 elements in simulating buckling behavior of cylindrical shells in Ref. [36]. Furthermore, quadratic shell elements (Shell281) are also considered for the comparison. Shell281 has eight nodes and 6-DOFs at each node.

For better representation of the obtained results, non-dimensional critical buckling, $L_K$=$12P_{\mathrm{c}}b^2(1-\nu^2)/E\pi^2t_{\mathrm{h}}^2$ and curvature, $Z$=$b^2\sqrt{1-\nu^2}/r_{\mathrm{c}}t_{\mathrm{h}}$, parameters are adopted from Ref. [51], where $P_{\mathrm{c}}$ is the critical stress. Aspect ratio of the shell is assumed as $a/b$=2.0. The radius of curvature $r_{\mathrm{c}}/b$ is varied from 5.0 to 63.0. $r_{\mathrm{c}}/b$=63.0 case corresponds to almost flat plate case. The shell thickness is $t_{\mathrm{h}}/b$=0.015 and the Poisson's ratio is $\nu$=0.3. The stiffener's web thickness, $t_{\mathrm{w}}$ is assumed to be same as the shell thickness, and the stiffener web height is varied as $h_{\mathrm{w}}/b$=0.15 and 0.2.

Before proceeding curvilinear shell assemblies, which are target structures in the present paper, 6-DOFs shell formulation in convected coordinates is compared with the 5-DOFs shell formulation for shallow shell problems under simply supported BCs, which were given by Ref. [36]. For the comparison, converged nodal density (41×81) in Ref. [36] is adopted. The results for present 6-DOFs formulation and reference values are provided in Table 1.

**Table 1** Buckling coefficients $L_K$ for shallow shells under simply supported condition ($a/b$=2.0).

| $r_{\mathrm{d}}/b$ | $Z$ | 6-DOFs (present) | 5-DOFs [36] | FEM [36] | Ref. [52] |
|---|---|---|---|---|---|
| 5.0 | 12.719 | 5.648 | 5.647 | 5.644 | 5.642 |
| 7.5 | 8.479 | 4.741 | 4.741 | 4.735 | 4.734 |
| 11.5 | 5.530 | 4.298 | 4.298 | 4.296 | 4.291 |
| 17.5 | 3.634 | 4.107 | 4.107 | 4.107 | 4.100 |
| 27.5 | 2.313 | 4.019 | 4.019 | 4.021 | 4.012 |
| 63.0 | 1.009 | 3.971 | 3.971 | 3.973 | 3.964 |

It is clearly seen in Table 1 that 6-DOFs meshfree formulation reveals almost the same buckling coefficients with 5-DOFs formulation for curvilinear surfaces. Furthermore, buckling mode shapes are exactly same with those of Ref. [36], they are therefore not given here. We may expect such same results for 6-DOFs and 5-DOFs shell formulation in case of single (isolated) shells. As for the shell assemblies (stiffened shells) as shall be discussed next, the 6-DOFs shell formulation is necessary.

### 5.1 Stiffened shallow shells

Buckling behavior of stiffened shallow shells is investigated. One single stiffener located on mid-part of the shell along the longitudinal direction is considered. Keeping the shell aspect ratio constant, while varying the curvature and the stiffener size, the buckling loads and modes are obtained. Modeling of the shallow shells with a straight stiffener is schematically illustrated in Fig.4.

In the given figure, $a$ denotes the length of the shallow shells, while $b$ is the breadth of curved side of the shell. $r_{\mathrm{c}}$ is the radius of curvature. $h_{\mathrm{w}}$ is the web height measured from the mid-thickness surface of the shell, and $t_{\mathrm{w}}$ is the web thickness. Simply supported BCs are considered for all edges including the stiffener tip, which means the displacements in $X_2$-direction are constrained. In order to suppress the rigid body motion, mid-point nodes on the longitudinal edges are constrained against the displacements in $X_3$-direction. Furthermore, lower corner point in Fig.4 is constrained against the displacements in $X_1$-direction. Two flat plates, which constitute the shell and the stiffener, are generated first. Then, the flat plate representing the stiffener is rotated so as to be orthogonal to the mother plate. All DOFs of the coinciding nodes are synchronized employing SKs. This concept has

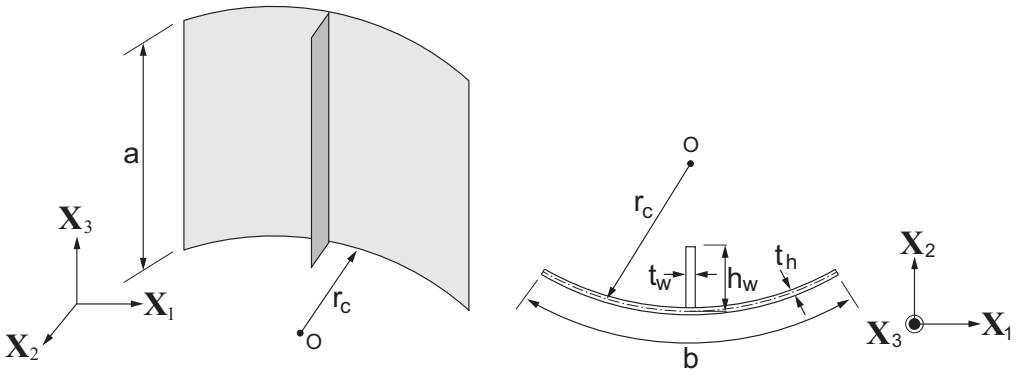


**Fig. 4** Representative modeling of the stiffened shallow shell.

been discussed extensively in our previous study [38]. A special mapping, which is same as Ref. [36], is adopted to transform the mother flat plate into a shallow shell.

As for convergence of the present meshfree formulation, a shallow shell model with a straight stiffener is analyzed. The most curved case, that is $r_c/b$=5.0, is considered. The web height is taken as $h_w/b$=0.2. Element edge length for the FEM computations is varied as $b/20$, $b/30$ and $b/40$. As for the meshfree computations, the nodal division is considered to be same as the element edge lengths of FEM models. The error is defined as $Error(\%)$=|Reference−Numer.|/Reference×100. Here, "Numer." denotes the results obtained by either present formulation or FEM. As for the reference result, fully converged FEM result employing quadratic shell elements (Shell281) is considered. In the fully converged FEM, total number of nodes is 18,321, obtained by setting element edge length as $b/50$. In this case, the critical buckling coefficient is $L_k$=15.8132. In the error computation, this fully converged result is adopted as the reference value. On the other hand, total numbers of nodes in the meshfree models are 1,066, 2,318 and 4,050 for $b/20$, $b/30$ and $b/40$ divisions, respectively. Assuming $b$=1.0, the results of convergence study for present meshfree formulation and FEM employing different element formulations, namely, linear and quadratic elements, are given in Table 2. In the given table, "MFree" denotes the results obtained by present formulation.

**Table 2** Convergence for stiffened shallow shells under simply supported condition ($r_c/b$=5.0, $h_w/b$=0.2).

| | Buckling coefficients ($L_k$) | | | Error (%) | | |
|---|---|---|---|---|---|---|
| Division | MFree | FEM (Shell181) | FEM (Shell281) | MFree | FEM (Shell181) | FEM (Shell281) |
| $b/20$ | 15.9202 | 16.2888 | 15.8175 | 0.6767 | 3.0072 | 0.0271 |
| $b/30$ | 15.9029 | 16.0888 | 15.8136 | 0.5667 | 1.7427 | 0.0024 |
| $b/40$ | 15.7906 | 16.0042 | 15.8132 | 0.1430 | 1.2077 | 0.0001 |

It is evident in Table 2 that the errors for the developed meshfree method are much lower than those of FEM with linear elements. The relative errors for present formulation are lower than 1% for all division cases, while the relative errors for FEM with linear elements are higher than 1% for all division cases. Furthermore, the accuracy of FEM with linear elements is studied by adopting very fine mesh, in which the element edge length is set as $b/150$. In this case, the relative error for linear shell elements is 0.1930%, which is still greater than that of present method with nodal division of $b/40$. Such difference may be attributed the difference in the element formulation and the numerical integration scheme.

On the other hand, it can be readily observed that the FEM with quadratic elements converges rapidly. The relative error for quadratic elements between the fully converged and the coarsest case is much lower than those of present method and linear shell elements. This could be explained by the merits of local property and quadratic approximation functions in FEM. Based on the results of the convergence analysis, the nodal distance, $b/40$, provides sufficiently accurate results in the meshfree buckling analysis; this division is then chosen for subsequent meshfree computations of the stiffened shallow shells. The obtained meshfree results for the critical buckling coefficients and modes

are compared with the fully converged FEM results. In addition, higher order buckling loads are also presented for the most curved and almost flat cases.

The comparative results for two aforementioned approaches are presented in Table 3. There are two important points that can be observed from Table 3. As expected, the first point is that the developed meshfree method offers acceptable results of the critical buckling coefficients in comparison with the FEM-based reference solutions. The second point lies in the fact that the present formulation can gain good results even if the number of nodes is smaller than those of the fully converged FEM. In addition to the higher order approximation functions, the advanced numerical integration techniques, *i.e.*, SCNI and SSCI for the plate - stiffener connections enable to obtain good agreement between the results such that the maximum error between the meshfree and quadratic FEM is 0.221%, which is observed in $r_c/b$=63.0, $h_w/b$=0.2 case.

**Table 3** Critical buckling coefficients $L_K$ for stiffened shallow shells under simply supported condition.

| | $h_w/b = 0.15$ | | | $h_w/b = 0.2$ | | |
|---|---|---|---|---|---|---|
| $r_c/b$ | MFree | FEM (Shell181) | FEM (Shell281) | MFree | FEM (Shell181) | FEM (Shell281) |
| 5.0 | 16.743 | 16.771 | 16.743 | 15.791 | 15.844 | 15.813 |
| 7.5 | 16.386 | 16.405 | 16.378 | 15.542 | 15.562 | 15.533 |
| 11.5 | 16.224 | 16.236 | 16.210 | 15.430 | 15.437 | 15.408 |
| 17.5 | 16.157 | 16.165 | 16.140 | 15.388 | 15.388 | 15.359 |
| 27.5 | 16.129 | 16.135 | 16.109 | 15.372 | 15.369 | 15.340 |
| 63.0 | 16.115 | 16.120 | 16.094 | 15.368 | 15.363 | 15.334 |

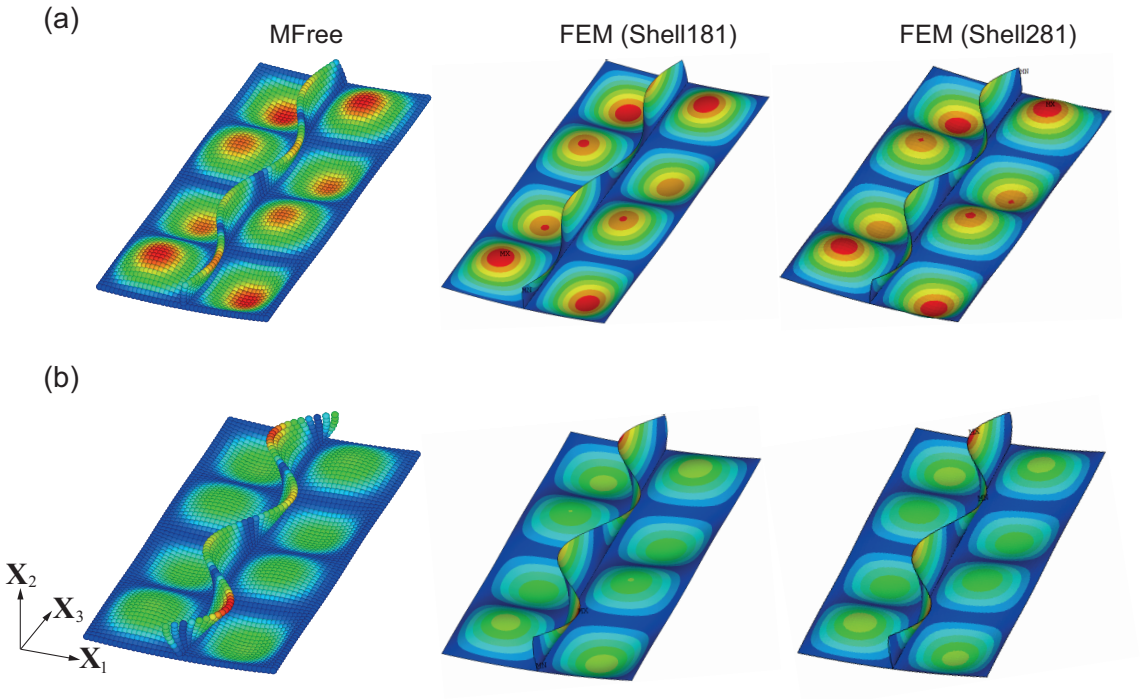


**Fig. 5** Critical buckling mode shapes for $r_c/b$=5.0: (a) $h_w/b$=0.15, (b) $h_w/b$=0.2.

The critical buckling mode shapes for the most curved ($r_c/b$=5.0) and almost flat ($r_c/b$=63.0) cases are given in Figs.5 and 6, respectively. Fig.5 indicates a good agreement between MFree and FEM in terms of critical buckling mode shapes regardless of the stiffener size. In case of $h_w/b$=0.15, buckling deflections occur both in shell and stiffener almost in the same magnitude. On the other hand, the magnitude of deflections in the stiffener is larger than that of the shell for $h_w/b$=0.2. This is because

the stiffener becomes slender owing to the larger height to thickness ratio without stiffener flange. This is also reason why the critical buckling coefficients are lower than that of $h_w/b$=0.15 case.

As can be seen in Fig.6(a), the buckling deflections obtained by MFree and FEM for the $h_w/b$=0.15 case are reverse to each other. Such reverse buckling deflection may be attributed to the reference coordinate system chosen for FEM computations. Both meshfree and FEM models are generated in global Cartesian coordinates, and very good agreement is achieved between the mode shapes except the ones by FEM given in Fig.6(a). To investigate the possible reason, the reference coordinate system of FEM has been shifted from Cartesian to cylindrical coordinates. It is interestingly found that the mode shapes by FEM become the same as one obtained by proposed meshfree method as indicated in Fig.7.

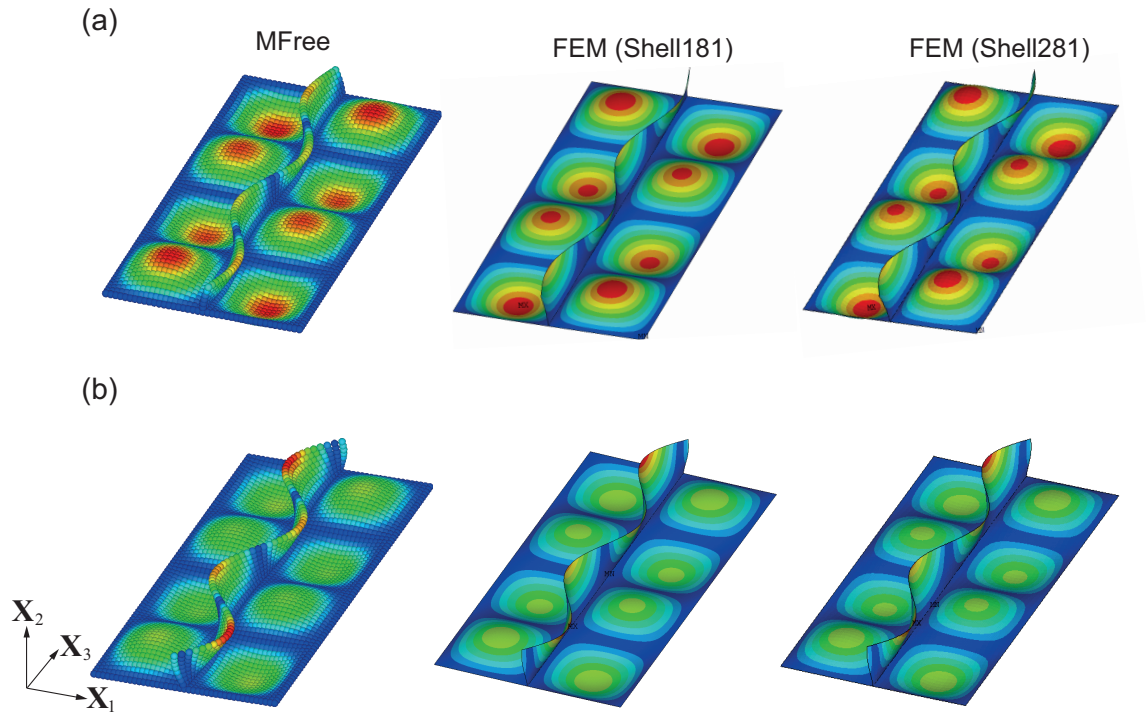


**Fig. 6** Critical buckling mode shapes for $r_c/b$=63.0: (a) $h_w/b$=0.15, (b) $h_w/b$=0.2.

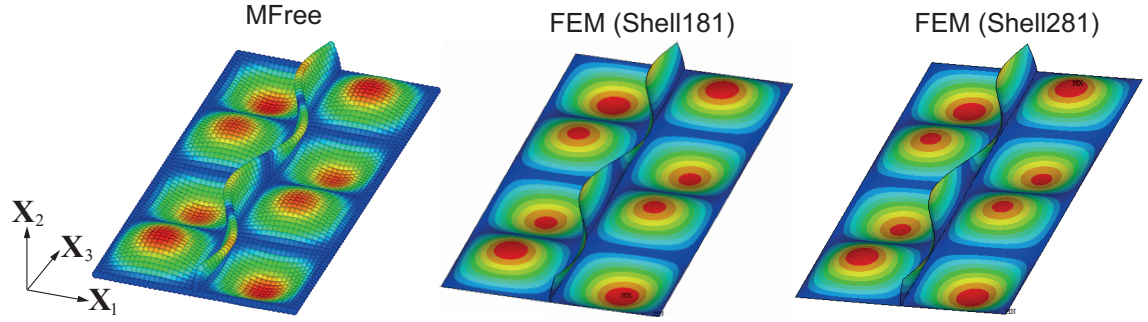


**Fig. 7** Critical buckling mode shapes for $r_c/b$=63.0, $h_w/b$=0.15 (FEM results in cylindrical coordinates).

In case of $h_w/b$=0.2 in Fig.6(b), magnitude of buckling deflection in the stiffener is larger than that of the shallow shell. In addition, the buckling deflection in the shallow shell is larger for $r_c/b$=63.0 case than that of $r_c/b$=5.0. This may be explained by the difference in the curvatures since the shells with

higher curvature are more resistant against buckling, see Table 1. This phenomenon is also observed in Table 3 so that the critical buckling coefficients decrease as increase of the radius of curvature for the same stiffener size. Although higher order buckling modes and loads do not have much physical meaning in practices, they could be examined to check the performance of the methods. The results are hence presented in Tables 4 and 5 for $r_c/b$=5.0 and $r_c/b$=63.0 cases, respectively.

**Table 4** Higher order buckling coefficients $L_K$ for $r_c/b$=5.0.

| | $h_w/b = 0.15$ | | | $h_w/b = 0.2$ | | |
|---|---|---|---|---|---|---|
| Mode | MFree | FEM (Shell181) | FEM (Shell281) | MFree | FEM (Shell181) | FEM (Shell281) |
| $1^{st}$ | 16.743 | 16.771 | 16.743 | 15.791 | 15.844 | 15.813 |
| $2^{nd}$ | 17.528 | 17.570 | 17.538 | 16.096 | 16.329 | 16.296 |
| $3^{rd}$ | 17.901 | 17.912 | 17.887 | 17.018 | 17.038 | 17.010 |
| $4^{th}$ | 19.534 | 19.595 | 19.565 | 18.089 | 19.055 | 19.022 |

Not surprisingly, the higher order buckling coefficients gained by MFree match well the reference FEM results, particularly with the quadratic elements. However, it must be noted that the higher order buckling modes and loads are very sensitive to discretization of the model aside to the element formulation since higher order buckling modes may become complicated for complex geometries. It is observed that the difference between 4th order buckling coefficients obtained by present formulation and FEM becomes slightly large for $r_c/b$=5.0, $h_w/b$=0.2 case. In this case, magnitude of buckling deflection in the stiffener is much larger than that of shallow shell owing to the larger web height/thickness ratio as well as small radius of curvature. As for the almost flat plate case ($r_c/b$=63.0), agreement between the FEM with linear elements and present meshfree formulation becomes well compared to higher curvature cases.

**Table 5** Higher order buckling coefficients $L_K$ for $r_c/b$=63.0.

| | $h_w/b = 0.15$ | | | $h_w/b = 0.2$ | | |
|---|---|---|---|---|---|---|
| Mode | MFree | FEM (Shell181) | FEM (Shell281) | MFree | FEM (Shell181) | FEM (Shell281) |
| $1^{st}$ | 16.115 | 16.120 | 16.094 | 15.368 | 15.363 | 15.334 |
| $2^{nd}$ | 16.914 | 16.926 | 16.899 | 15.884 | 15.859 | 15.822 |
| $3^{rd}$ | 17.337 | 17.340 | 17.315 | 16.450 | 16.461 | 16.435 |
| $4^{th}$ | 18.841 | 18.872 | 18.845 | 17.992 | 17.928 | 17.928 |

In conclusion, the present formulation simulates buckling behavior of stiffened shallow shells well. If the stiffener size is smaller, *i.e.*, $h_w/b$ <0.15, the overall buckling (simultaneous flexural buckling of shell and the stiffener) may take place, and the shell formulation for the stiffeners may not be crucial since the stiffener will deform like a beam. On the other hand, the local buckling of plate/stiffener occurs in case of larger stiffener sizes, *i.e.*, $h_w/b \geq$0.15, which is the scope of the present study. In the latest cases, the modeling of stiffeners by shell formulation is crucial for the accurate buckling load and mode estimations.

### 5.2 Flat plate with curvilinear stiffeners

The buckling behavior of a flat plate with curvilinear stiffeners of different configurations is investigated. At first, one curvilinear stiffener case is considered. Then, the critical buckling loads and modes of a flat plate with two curvilinear stiffeners are obtained. In these problems, as a first step, both plate and stiffeners are modeled as flat plates, then the stiffener part is mapped into a curvilinear surface by mapping. All DOFs of the coinciding nodes along the plate - stiffener connections are synchronized to each other. Furthermore, SSCI is adopted to simulate higher stress gradients along the plate - stiffener connections. Flat plate models with curvilinear stiffeners are schematically illustrated in Fig.8. Flat plate model with one stiffener is called as "Model A" while the flat plate model with two stiffeners is called as "Model B". Those models have been previously analyzed by FEM in Ref. [20] adopting beam

elements for modeling of the stiffeners. Simply supported BCs are imposed to all edges of the flat plate keeping the stiffener tips free so that the displacements in $X_3$-direction are suppressed. To suppress the rigid body motion of the model, the displacements in $X_1$-direction are constrained at mid-point nodes of edges II and IV, as well as the displacements in $X_2$-direction are constrained at mid-point nodes of edges I and III. Moreover, all edges including stiffener tips are assumed to be remain straight. Both sided uniaxial thrust load is applied in $X_2$-direction on the edges II and IV. The dimensions for the Model A are $a$=$b$=120 mm. The plate thickness $t_\mathrm{h}$ is 1.2 mm. The stiffener dimensions are assumed as $h_\mathrm{w}$=12.58 mm and $t_\mathrm{w}$=1.14 mm. The material properties are taken as $E$=69 GPa and $\nu$=0.3.

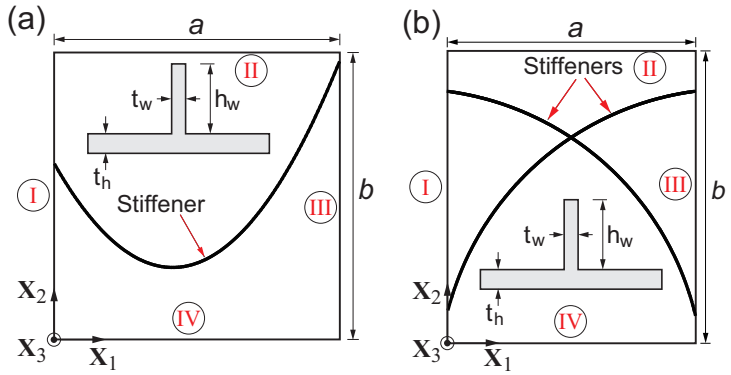


**Fig. 8** Flat plate models with curvilinear stiffeners: (a) Model A, (b) Model B.

In Fig.8, coordinates of the stiffener's points for Model A are obtained by $X_2$=$0.0176(X_1 - 50)^2 + 30$. On the other hand, the coordinates of the stiffeners for Model B are determined by $X_2$=$\sqrt{720^2 - (X_1 - 700)^2} - 100$ and $X_2$=$\sqrt{720^2 - (X_1 + 93.1)^2} - 100$. The dimensions for the Model B are $a$=606.9 mm, $b$=711.2 mm, and the plate thickness $t_\mathrm{h}$ is 6.07 mm. As for the stiffener dimensions, $h_\mathrm{w}$=63.62 mm and $t_\mathrm{w}$=6.78 mm assumptions are made. The material properties are taken as $E$=73 GPa and $\nu$=0.33. Buckling parameter, $k$=$\sigma_{cr} a^2 t_\mathrm{h}/\pi^2 D$, is adopted from Ref. [20] to present the results, in which $D$ is flexural stiffness of the flat plate, while $\sigma_{cr}$ denotes the buckling stress. In case of Model A, 65 nodes are located along $X_1$ and $X_2$ directions. As for the Model B, 55 and 65 nodes are located along $X_1$ and $X_2$ directions, respectively. For the stiffener webs, 7 and 8 nodes are put for Model A and Model B, respectively. Total numbers of nodes are 5,272 for Model A, and 5,137 for Model B. As for the FEM results, fully converged results are considered. Then, the buckling parameters for flat plate models with curvilinear stiffeners are compared in Table 6 for present method and FEM employing linear and quadratic elements.

**Table 6** Buckling coefficients $k$ for flat plate models with curvilinear stiffeners.

| | Model A | | | Model B | | |
|---|---|---|---|---|---|---|
| Mode | MFree | FEM (Shell181) | FEM (Shell281) | MFree | FEM (Shell181) | FEM (Shell281) |
| $1^{st}$ | 8.759 | 8.776 | 8.772 | 10.668 | 10.644 | 10.639 |
| $2^{nd}$ | 9.571 | 9.489 | 9.492 | 19.168 | 19.278 | 19.265 |
| $3^{rd}$ | 17.764 | 17.636 | 17.635 | 24.339 | 24.105 | 24.058 |
| $4^{th}$ | 22.769 | 22.301 | 22.290 | 26.750 | 26.846 | 26.819 |

As seen in Table 6, good agreement is achieved between the critical buckling (1st mode) parameters. In addition, we can observe good correlation between higher order buckling parameters up to 4th mode. However, as stated before, higher order loads and modes heavily depend on the discretization aside the element formulation. By increasing the number of nodes in the meshfree model, good agreement can be achieved for higher order buckling parameters. Critical buckling mode shapes for Models A and B are given in Figs.9 and 10, respectively.

As can easily be observed from Figs.9 and 10 that both considered methods offer similar critical mode shapes for Model A and Model B, respectively. Even though the structure of Model B is compli-

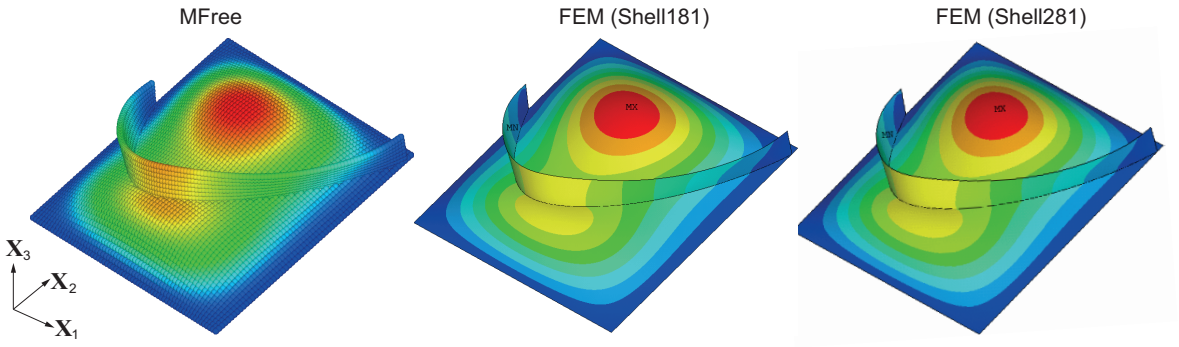


**Fig. 9** Critical buckling mode shapes of Model A obtained by MFree and FEM.

cated, the buckling mode is simpler, that is buckling deflection develop only in plate part, compared to the Model A. In case of Model A, deflection occurs in both plate and the stiffener, which is more complicated than that of Model B. Such phenomenon can be observed in Table 6, that is the difference between buckling coefficients obtained by present formulation and FEM for Model A becomes slightly larger than that of Model B. This could be attributed to more stable characteristic of Model B owing to the two stiffeners so that local buckling occurs only in plate. In practice, structures are designed so that the local bucking of plate takes place prior to stiffener buckling. Once stiffener buckling occurs, overall load bearing capacity of the structure might be lost.

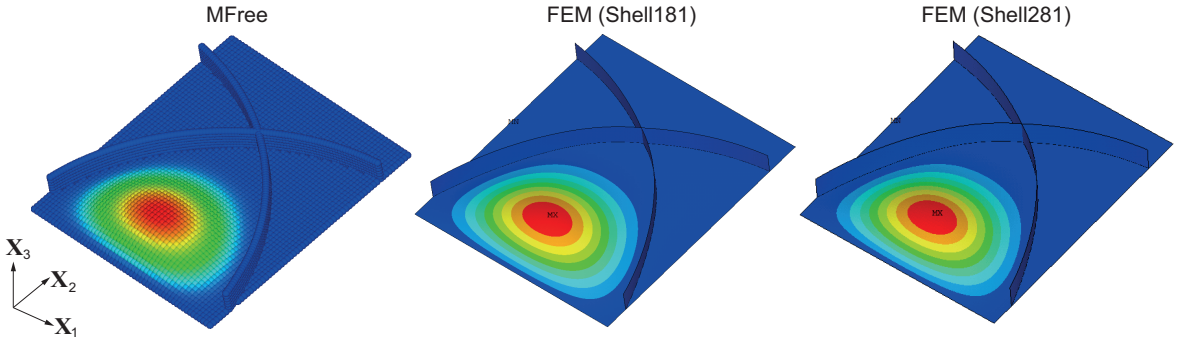


**Fig. 10** Critical buckling mode shapes of Model B obtained by MFree and FEM.

### 5.3 Twisted T-shaped structure

The last numerical example deals with a twisted T-shaped structure with uniform thickness [53] as schematically depicted in Fig.11. In this case, both web and flange have curvilinear surfaces. Both ends of the model are assumed to be clamped keeping the displacement in $X_1$-direction free but uniform at the loaded edge. Then, unit point load is applied at the intersection point of the web and flange in the $X_1$-direction. Material properties are taken as $E$=2 $\times$ $10^7$, and $\nu$=0.3. The model has no unit.

T-shaped structure is generated first by assembly of flat plates in a similar fashion with Ref. [38]. Then, the coordinates of the nodes are transformed by mapping functions into a twisted shape. Nodal division is considered as $(21 + 29) \times 101$ for $(h_w + b) \times L$ directions. Total number of nodes in the meshfree model is 5,050. As for the FEM results, fully converged results are considered.

As can be seen from Table 7, good agreement is achieved in terms of critical buckling stress obtained by present formulation and quadratic FEM. In Fig.12, critical mode shapes are provided, and the agreement between the critical mode shapes is excellent although the geometry is quite complex, which shows the present formulation is capable of representing buckling behavior of complicated curvilinear geometries. As for the higher order buckling stresses, the agreement between the present formulation

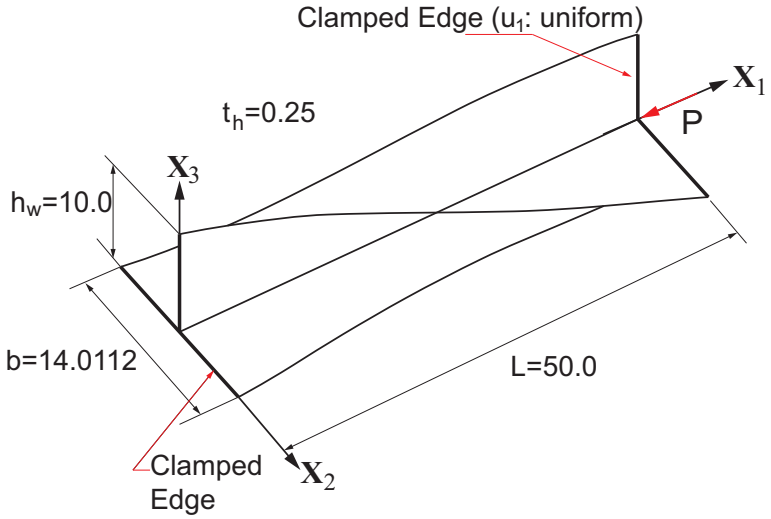


**Fig. 11** Geometric modeling and BCs for twisted T-shaped structure.

**Table 7** Buckling stresses for twisted T-shaped structure.

| Mode | MFree | FEM (Shell181) | FEM (Shell281) |
|---|---|---|---|
| $1^{st}$ | $4.204 \times 10^4$ | $4.221 \times 10^4$ | $4.208 \times 10^4$ |
| $2^{nd}$ | $4.220 \times 10^4$ | $4.238 \times 10^4$ | $4.225 \times 10^4$ |
| $3^{rd}$ | $4.363 \times 10^4$ | $4.373 \times 10^4$ | $4.360 \times 10^4$ |
| $4^{th}$ | $4.416 \times 10^4$ | $4.428 \times 10^4$ | $4.415 \times 10^4$ |

and the quadratic FEM is excellent while linear FEM suffers from modeling and simulating buckling of curvilinear geometries.

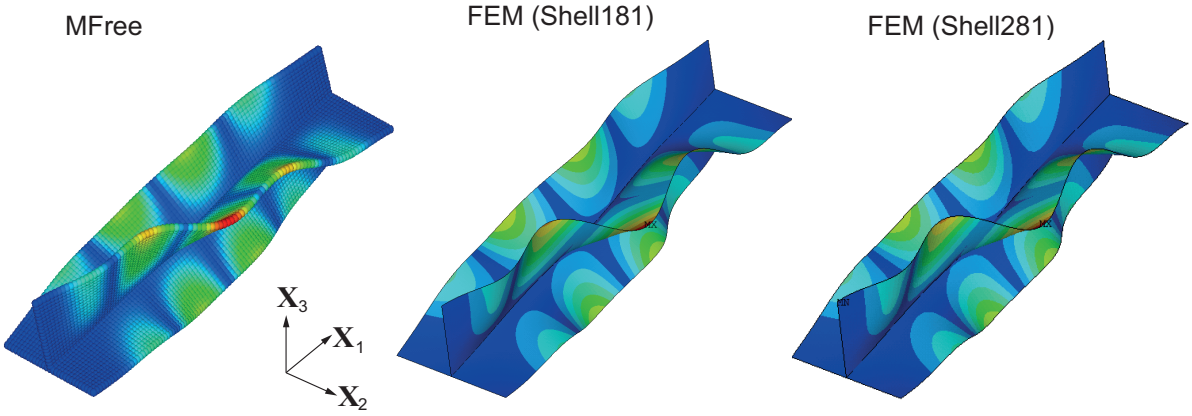


**Fig. 12** Critical buckling mode shapes for twisted T-shaped structure.

## 6 Conclusions

A series of meshfree buckling analysis is carried out to examine the buckling loads and modes of the stiffened plates with complex curvilinear surfaces, as well as to show the accuracy and effectiveness of the present meshfree formulation. Critical buckling modes and loads are obtained by both present method and fully converged FEM analyses employing linear (Shell181) and quadratic (Shell281) shell elements.

Present meshfree method reveals satisfactory results in terms of both buckling loads and modes. In a particular case, the buckling modes shapes obtained by the present method and FEM are reverse to each other even though the buckling coefficients are in good agreement.

As increase of curvature in shells, the agreement between the present meshfree method and quadratic FEM becomes well. On the other hand, we achieve good agreement between linear FEM and present method for small curvatures, which indicates that the present meshfree method can simulate the buckling behavior of curvilinear shell assemblies satisfactorily well, while linear FEM suffer from modeling and simulating the buckling behavior of highly curved shells.

## Acknowledgements

The authors are grateful to Mr. Ken-ichiro Yoshida and Mr. Kimihiro Taniguchi (Graduate School of Engineering, Hiroshima University) for their valuable comments and discussions.

## References

1. Mukhopadhyay, M., Mukherjee, A.: Finite element buckling analysis of stiffened plates. Comput. Struct. **34**, 795-803 (1990)
2. Jiang, W., Bao, G., Robert, J.C.: Finite element modeling of stiffened and unstiffened orthotropic plates. Comput. Struct. **63**, 105-117 (1997)
3. Sadek, E.A., Tawfik, S.A.: A finite element model for the analysis of stiffened laminated plates. Comput. Struct. **75**, 369-383 (2000)
4. Prusty, B.G., Satsangi, S.K.: Analysis of stiffened shell for ships and ocean structures by finite element method. Ocean Eng. **28**, 621-638 (2001)
5. Fujikubo, M., Yao, T.: Elastic local buckling strength of stiffened plate considering plate/stiffener interaction and welding residual stress. Mar. Struct. **12**, 543-564 (1999)
6. Stamatelos, D.G., Labeas, G.N., Tserpes, K.I.: Analytical calculation of local buckling and post-buckling behavior of isotropic and orthotropic stiffened panels. Thin-Walled Struct. **49**, 422-430 (2011)
7. Byklum, E., Steen, E., Amdahl, J.: A semi-analytical model for global buckling and postbuckling analysis of stiffened panels. Thin-Walled Struct. **42**, 701-717 (2004)
8. Brubak, L., Hellesland, J., Steen, E.: Semi-analytical buckling strength analysis of plates with arbitrary stiffener arrangements. J. Constr. Steel Res. **63**, 532-543 (2007)
9. Brubak, L., Hellesland, J.: Semi-analytical postbuckling and strength analysis of arbitrarily stiffened plates in local and global bending. Thin-Walled Struct. **45**, 620-633 (2007)
10. Fujikubo, M., Harada, M., Yao, T., Khedmati, M.R., Yanagihara, D.: Estimation of ultimate strength of continuous stiffened panel under combined transverse thrust and lateral pressure Part 2: Continuous stiffened panel. Mar. Struct. **18**, 411-427 (2005)
11. Paik, J.K., Seo, J.K.: Nonlinear finite element method models for ultimate strength analysis of steel stiffened-plate structures under combined biaxial compression and lateral pressure actions-Part II: Stiffened panels. Thin-Walled Struct. **47**, 998-1007 (2009)
12. Tanaka, S., Yanagihara, D., Yasuoka, A., Harada, M., Okazawa, S., Fujikubo, M., Yao, T.: Evaluation of ultimate strength of stiffened panels under longitudinal thrust. Mar. Struct. **36**, 21-50 (2014)
13. Ozdemir, M., Ergin, A., Yanagihara, D., Tanaka, S., Yao, T.: A new method to estimate ultimate strength of stiffened panels under longitudinal thrust based on analytical formulas. Mar. Struct. **59**, 510-535 (2018)
14. Paik, J.K., Thayamballi, A.K., Kim, B.J.: Large deflection orthotropic plate approach to develop ultimate strength formulations for stiffened panels under combined biaxial compression/tension and lateral pressure. Thin-Walled Struct. **39**, 215-246 (2001)
15. Paik, J.K., Lee, M.S.: A semi-analytical method for the elastic-plastic large deflection analysis of stiffened panels under combined biaxial compression/tension, biaxial in-plane bending, edge shear, and lateral pressure loads. Thin-Walled Struct. **43**, 375-410 (2005)
16. Seo, J.K., Song, C.H., Park, J.S., Paik, J.K.: Nonlinear structural behaviour and design formulae for calculating the ultimate strength of stiffened curved plates under axial compression. Thin-Walled Struct. **107**, 1-17 (2016)
17. Yao, T., Fujikubo, M.: Buckling and ultimate strength of ship and ship-like floating structures. Butterworth-Heinemann-Elsevier (2016)
18. Kapania, R.K., Li, J., Kapoor, H.: Optimal design of unitized panels with curvilinear stiffeners. AIAA 5th Aviation, Technology, and Operations Conference (ATIO). **3**, 1708-1737 (2005)
19. Tamijani, A.Y., Kapania, R.K.: Buckling and static analysis of curvilinearly stiffened plates using mesh-free method. AIAA Journal. **48**, 2739-2751 (2010)
20. Shi, P., Kapania, R.K., Dong, C.Y.: Vibration and buckling analysis of curvilinearly stiffened plates using finite element method. AIAA Journal. **53**, 1319-1335 (2015)
21. Zhao, W., Kapania, R.K.: Buckling analysis of unitized curvilinearly stiffened composite panels. Compos. Struct. **135**, 365-382 (2016)

22. Locatelli, D., Mulani, S.B., Kapania, R.K.: Wing-box weight optimization using curvilinear spars and ribs (SpaRibs). J. Aircraft. **48**, 1671-1684 (2011)
23. Mulani, S.B., Slemp, W.C.H., Kapania, R.K.: EBF3PanelOpt: An optimization framework for curvilinear blade-stiffened panels. Thin-Walled Struct. **63**, 13-26 (2013)
24. Qin, X.C., Dong, C.Y., Wang, F., Qu, X.Y.: Static and dynamic analyses of isogeometric curvilinearly stiffened plates. Appl. Math. Model. **45**, 336-364 (2017)
25. Qin, X.C., Dong, C.Y., Wang, F., Gong, Y.P.: Free vibration analysis of isogeometric curvilinearly stiffened shells. Thin-Walled Struct. **116**, 124-135 (2017)
26. Leheta, H.W., Badran, S.F., Elhanafi, A.S.: Ship structural integrity using new stiffened plates. Thin-Walled Struct. **94**, 545-561 (2015)
27. Liew, K.M., Wang, J., Ng, T.Y., Tan, M.J.: Free vibration and buckling analyses of shear-deformable plates based on FSDT meshfree method. J. Sound Vib. **276**, 997-1017 (2004)
28. Liew, K.M., Chen, X.L., Reddy, J.N.: Mesh-free radial basis function method for buckling analysis of non-uniformly loaded arbitrarily shaped shear deformable plates. Comput. Meth. Appl. Mech. Eng. **193**, 205-224 (2004)
29. Liew, K.M., Peng, L.X., Kitipornchai, S.: Buckling analysis of corrugated plates using a mesh-free Galerkin method based on first-order shear deformation theory. Comput. Mech. **38**, 61-75 (2006)
30. Liew, K.M., Peng, L.X., Kitipornchai, S.: Buckling of folded plate structures subjected to partial in-plane edge loads by the FSDT meshfree Galerkin method. Int. J. Numer. Meth. Eng. **65**, 1495-1526 (2006)
31. Bui, T.Q., Vo, D.Q., Zhang, C., Nguyen, D.D.: A consecutive-interpolation quadrilateral element (CQ4): Formulation and applications. Finite Elem. Anal. Des. **84**, 14-31 (2014)
32. Kang, Z., Bui, T.Q., Nguyen, D.D., Saitoh, T., Hirose S.: An extended consecutive-interpolation quadrilateral element (XCQ4) applied to linear elastic fracture mechanics. Acta Mech. **226**, 3991-4015 (2015)
33. Tanaka, S., Suzuki, H., Sadamoto, S., Imachi, M., Bui, T.Q.: Analysis of cracked shear deformable plates by an effective meshfree plate formulation. Eng. Fract. Mech. **144**, 142-157 (2015)
34. Tanaka, S., Suzuki, H., Sadamoto, S., Sannomaru, S., Yu, T.T., Bui T.Q.: J-integral evaluation for 2D mixed-mode crack problems employing a meshfree stabilized conforming nodal integration method. Comput. Mech. **58**, 185-198 (2016)
35. Tanaka, S., Suzuki, H., Sadamoto, S., Okazawa, S., Yu, T.T., Bui, T.Q.: Accurate evaluation of mixed-mode intensity factors of cracked shear-deformable plates by an enriched meshfree Galerkin formulation. Arch. Appl. Mech. **87**, 279-298 (2017)
36. Sadamoto, S., Ozdemir, M., Tanaka, S., Taniguchi, K., Yu, T.T., Bui, T.Q.: An effective meshfree reproducing kernel method for buckling analysis of cylindrical shells with and without cutouts. Comput. Mech. **59**, 919-932 (2017)
37. Yoshida, K., Sadamoto, S., Setoyama, Y., Tanaka, S., Bui, T.Q., Murakami, C., Yanagihara, D.: Meshfree flat-shell formulation for evaluating linear buckling loads and mode shapes of structural plates. J. Mar. Sci. Tech. **22**, 501-512 (2017)
38. Sadamoto, S., Tanaka, S., Taniguchi, K., Ozdemir, M., Bui, T.Q., Murakami, C., Yanagihara, D.: Buckling analysis of stiffened plate structures by an improved meshfree flat shell formulation. Thin-Walled Struct. **117**, 303-313 (2017)
39. Chen, J.S., Wang D.: A constrained reproducing kernel particle formulation for shear deformable shell in Cartesian coordinates. Int. J. Numer. Meth. Eng. **68**, 151-172 (2006)
40. Sadamoto, S., Yoshida, K., Tanaka, S.: Modeling of plate structures for Galerkin meshfree methods (2nd report: Geometrical non-linear analysis). Trans. Japan Soc. Mech. Eng. **81**, 1-12 (2015) (in Japanese)
41. Sadamoto, S., Tanaka, S., Okazawa, S.: Elastic large deflection analysis of plates subjected to uniaxial thrust using meshfree Mindlin-Reissner formulation. Comput. Mech. **52**, 1313-1330 (2013)
42. Chen, J.S., Wang, H.P.: New boundary condition treatments in meshfree computation of contact problems. Comput. Meth. Appl. Mech. Eng. **187**, 441-468 (2000)
43. Wang, D., Chen, J.S.: A Hermite reproducing kernel approximation for thin-plate analysis with sub-domain stabilized conforming integration. Int. J. Numer. Meth. Eng. **74**, 368-390 (2008)
44. Wang, D., Peng, H.: A Hermite reproducing kernel Galerkin meshfree approach for buckling analysis of thin plates. Comput. Mech. **51**, 1013-1029 (2013)
45. Wang, D., Song C., Peng, H.: A Circumferentially Enhanced Hermite Reproducing Kernel Meshfree Method for Buckling Analysis of Kirchhoff-Love Cylindrical Shells. Int. J. Struct. Stabil. Dynam. **15**, 1450090 (2015)
46. Wang, D., Wu, J.: An efficient nesting sub-domain gradient smoothing integration algorithm with quadratic exactness for Galerkin meshfree methods. Comput. Meth. Appl. Mech. Eng. **298**, 485-519 (2016)
47. Chen, J.S., Wu, C.T., Yoon, S., You, Y.: A stabilized conforming nodal integration for Galerkin mesh-free methods. Int. J. Numer. Meth. Eng. **50**, 435-466 (2001)
48. Kanok-Nukulchai, W.: A simple and efficient finite element for general shell analysis. Int. J. Numer. Meth. Eng. **14**, 179-200 (1979)
49. Noguchi, H., Kawashima, T., Miyamura, T.: Element free analyses of shell and spatial structures. Int. J. Numer. Meth. Eng. **47**, 1215-1240 (2000)
50. ANSYS vers. 17.2: User's Guide (2016)
51. Gerard, G., Becker, H.: Handbook of structural stability part III: buckling of curved plates and shells. NACA TN 3783 (1957)
52. Baiz, P.M., Aliabadi, M.H.: Linear buckling analysis of shear deformable shallow shells by the boundary domain element method. Comput. Model. Eng. Sci. **13**, 19-34 (2006)
53. Chróścielewski, J., Witkowski, W.: Four-node semi-EAS element in six-field nonlinear theory of shells. Int. J. Numer. Meth. Eng. **68**, 1137-1179 (2006)